Acta Materialia 280 (2024) 120295

Contents lists available at ScienceDirect

Acta Materialia

journal homepage: www.elsevier.com/locate/actamat

Oxygen-induced decomposition of the body-centered cubic HfNbTaTiZr high-entropy alloy

Régis Poulain [a,*], Maik Rajkowski [b], Yujun Zhao [b], Parham Gemagami [b], Benoît Appolaire [c,d], Stephan Laube [e], Alexander Kauffmann [e], Loïc Perrière [a], Jean-Philippe Couzinié [a], Tong Li [b], Guillaume Laplanche [b]

[a] Université Paris Est, Institut de Chimie et des Matériaux Paris-Est (UMR7182), CNRS, UPEC, 2-8 rue Henri Dunant, F-94320, Thiais, France
[b] Institute for Materials, Ruhr University Bochum, Universitätsstr. 150, D-44780 Bochum, Germany
[c] Université de Lorraine, Institut Jean Lamour, Campus ARTEM, Allée André Guinier, F-54011 Nancy, France
[d] Labex DAMAS, Université de Lorraine, France
[e] Institute for Applied Materials (IAM-WK), Karlsruhe Institute of Technology (KIT), Kaiserstraße 12, 76131, Karlsruhe, Germany

ARTICLE INFO

Keywords:
TiZrNbHfTa
HEA
Orientation relationship
Interstitials
Heterogeneous precipitation
Morphology

ABSTRACT

The factors affecting the stability of an initially single-phase body-centered cubic (BCC) HfNbTaTiZr solid solution are investigated by heat treatments at 900 °C up to 1000 h in different atmospheres. The BCC solid solution is stable but oxygen (O) contamination originating from the aging atmosphere leads to the co-precipitation of an O-enriched hexagonal close-packed (HCP) Hf-Zr-rich phase and a second Nb-Ta-rich BCC phase. As O from the atmosphere diffuses from the surface to the core of the sample at a much faster rate along grain boundaries than through the grain interior, this results in an inhomogeneous distribution of precipitates, which formed at grain boundaries by a monotectoid reaction. In contrast, coincidence-site-lattice boundaries are not affected by this transformation owing to their lower diffusivities and lower capacity for heterogeneous nucleation. Similar phases were observed in a HfNbTaTiZr enriched with 3 at.% O, thus confirming the role of oxygen in phase stability.

In both alloys, the orientation relationship (OR) between the HCP and BCC phases is predominantly of Burgers type but our analyses further revealed the presence of two minor ORs. More interestingly, both alloys exhibit rod-shaped HCP precipitates in contrast to the plate-shaped precipitates observed in conventional Ti and Zr-based alloys. This result can be rationalized by calculations of elastic strain energy density, which suggest that the rods should grow along $\langle 100 \rangle_{BCC}$ to minimize the elastic strain energy. Deviations of up to 20° from this theoretical direction were observed and are likely related to relaxation by misfit dislocations or by plastic deformation.

1. Introduction

The HfNbTaTiZr high-entropy alloy (HEA) is a five element alloy that was designed by Senkov et al. [1,2]. It can form a single-phase body-centered cubic (BCC) solid solution when it is annealed at sufficiently high temperatures, and it remains in this state at room temperature when quenched in air. This alloy is one of the few BCC HEAs that is ductile and malleable at room temperature [3]. Owing to these properties, the HfNbTaTiZr alloy has been successfully processed using various techniques including cold rolling [3], high-pressure torsion [4,5], as well as powder metallurgy processes such as spark plasma sintering [6] and additive manufacturing [7,8]. Due to the good malleability of the HfNbTaTiZr alloy, its cast microstructure can be broken up by cold working followed by recrystallization annealing to establish well-defined grain sizes. These are some of the reasons why the HfNbTaTiZr alloy is one of the most thoroughly investigated BCC HEAs in terms of mechanical [3,9] and physical properties [10-13], plastic behavior at low [14-18] and elevated temperatures [19-23], diffusion kinetics [24], and oxidation resistance [25,26]. Regarding its phase stability, Schuh et al. [4] first discovered that the severely plastically deformed BCC HfNbTaTiZr solid solution decomposes into multiple phases when annealed at intermediate temperatures, resulting in

* Corresponding author.
E-mail address: regis.poulain@cnrs.fr (R. Poulain).

https://doi.org/10.1016/j.actamat.2024.120295
Received 12 March 2024; Received in revised form 19 July 2024; Accepted 14 August 2024
Available online 15 August 2024

embrittlement at room temperature. At the same time, Chen et al. [27] investigated a cold-rolled and recrystallized HfNbTaTiZr alloy (5 μm < grain size < 60 μm) and found it to decompose below 900 °C into a Zr-Hf-rich hexagonal close-packed (HCP) phase and a Nb-Ta-rich BCC solid solution, consistent with the work of Stepanov et al. [28]. In the meantime, other groups experimentally investigated the phase stability of this alloy, and large discrepancies were reported. For instance, while Chen et al. [27] found that the alloy forms a stable single-phase solid solution above 900 °C, Yang et al. [29] reported the presence of secondary phases up to 1450 °C and Maiti et al. [30] observed the formation of short-range clustering during annealing at 1800 °C leading to the minor formation of HCP phase after 4 days.

The first objective of the present work is to show that these discrepancies may be related to the presence of oxygen (O) that strongly affects the phase stability of the HfNbTaTiZr HEA. This study also aims at investigating key crystallographic aspects of the phase transformation ($BCC_1 \rightarrow BCC_2 + HCP$). For instance, the preliminary transmission electron microscopy (TEM) results of Chen et al. [27] suggested that the orientation relationship (OR) between the HCP and BCC phases corresponds to the classical Burgers OR (BOR) [31]. However, it is worth mentioning that the authors did not report any statistical information, suggesting that their data were only representative of a local area within a single grain. In the present work, our second objective is to improve the statistics by investigating a much larger area, different grains, and colonies of precipitates by electron backscatter diffraction (EBSD). As will be shown in this article, we confirm that the major OR between HCP and BCC is the BOR but we also uncover two additional minor ORs that have not been reported so far. Further crystallographic aspects that will be investigated in the present work are related to the following observations from literature. (1) Previous studies have reported that precipitation occurs heterogeneously at grain boundaries, but some of them remain devoid of precipitates, e.g. [27]. (2) The microstructure of the HfNbTaTiZr alloy after precipitation is peculiar and strongly differs from those observed in traditional and initially single-phase BCC Ti and Zr alloys. While HCP platelets are formed in binary Ti and Zr solid solutions, rod-shaped precipitates grow in the HfNbTaTiZr alloy. Analytical calculations of the orientation-dependent, elastic strain energy associated with the phase transformation ($BCC_1 \rightarrow BCC_2 + HCP$), assuming coherent interfaces suggest that the change from plate-like to rod-like morphology can be rationalized by the differences in lattice parameters of the HCP and BCC phases between the binary and the quinary alloys. The growth direction of the rod precipitates, analyzed by a trace analysis, is distributed between ⟨100⟩ and ⟨311⟩ directions with significant deviations between precipitate directions within the same colonies. In our opinion, the precipitates initially grow along ⟨100⟩ as suggested by the calculations and eventually deviate from this direction when the large misfit is relaxed by bulk plasticity or interfacial dislocations.

2. Experimental methods

2.1. Processing of single-phase BCC HfNbTaTiZr and HfNbTaTiZr-3%O alloys

To investigate the effect of O on the phase stability of the HfNbTaTiZr alloy, two alloys with and without O additions were produced, i.e., HfNbTaTiZr and HfNbTaTiZr-3 %O (doped with 3 at.% O). The HfNbTaTiZr alloy with nominal composition $Hf_{20}Nb_{20}Ta_{20}Ti_{20}Zr_{20}$ in at.% was produced by arc melting and homogenization, followed by cold rolling (~80 % total thickness reduction with a thickness reduction of 100 to 200 μm per pass) and annealing at 1373 K for 5 h under He stream, as reported elsewhere [32]. After this last heat treatment, the alloy was found to be single-phase BCC with low impurity levels determined at a commercial laboratory (0.27 at.% O and 0.10 at.% N measured by inert gas fusion method, and ~0.07 at.% C measured by infrared absorption method [13], see Table 1), nearly equiaxed grains (grain size: ~70 μm) and random texture (both determined using EBSD in Ref. [13]).

The HfNbTaTiZr-3 %O alloy was arc melted in an AM/0.5 furnace supplied by Edmund Bühler GmbH (Germany) and equipped with a non-consumable W electrode. Pure metals (purity: ≥ 99.95 wt.%, EvoChem GmbH, Germany) and TiO_2 (purity: 99.95 %, chemPur GmbH, Germany) were used for synthesis. The processing chamber was evacuated and filled with Ar three times before a high vacuum was established. Finally, the Ar pressure in the chamber was set to ~600 mbar and maintained throughout the melting process. The raw materials were melted in a water-cooled Cu crucible. The button obtained after solidification was flipped and remelted five times before the final melt was drop cast into a rod shape (diameter: 13 mm, height: 90 mm). The as-cast rod was then encapsulated in an evacuated fused silica ampoule and annealed at 1200 °C for 48 h followed by water quenching. This last heat treatment resulted in a single-phase BCC solid solution with a mean grain size of ~50 μm and a random texture as confirmed by electron backscatter diffraction (EBSD).

Similar methods were employed to determine the compositions of the HfNbTaTiZr and HfNbTaTiZr-3 %O alloys. The composition of the latter was determined in-house and at a commercial laboratory (Revierlabor GmbH, Germany) using inductively coupled plasma-optical emission spectrometry (ICP-OES) and X-ray fluorescence analysis (XRFA) for metallic elements, respectively, while O and N contents were analyzed employing carrier gas hot extraction. Both measurements yielded similar values with an average composition reported in Table 1. Additional energy dispersive X-ray spectroscopy (EDS) analyses revealed that both alloys are chemically homogeneous at the microscale. However, we cannot exclude nanoscale chemical fluctuations and/or clustering. These aspects will be addressed in a forthcoming systematic study using atom probe tomography (APT).

2.2. Heat treatments, metallographic preparation, microstructural, chemical, and crystallographic analyses

Pieces of the HfNbTaTiZr and HfNbTaTiZr-3 %O alloys (dimensions: 4 mm × 2 mm × 1 mm) were individually wrapped in Ta foil and encapsulated with a Ti getter under ~300 mbar of Ar, annealed at 900 °C for up to 1000 h and water quenched. To investigate how the annealing conditions affect the stability of the BCC solid solution, additional heat treatments were performed under vacuum (3×10^{-5} mbar) without wrapping the specimens in Ta foil.

To catch the potential presence of heterogeneities (e.g., precipitation at the sample surface without any precipitation in the sample core), cross-sections including the sample surface were prepared, see Fig. 1a for the HfNbTaTiZr alloy. For this purpose, the pieces were embedded edge on in epoxy, ground, polished to 1 μm, and prepared for 24 h in a Buehler Vibromet 2 using a mixture of deionized water and polishing

Table 1
Chemical compositions (in at.%) of the HfNbTaTiZr and HfNbTaTiZr-3 %O high-entropy alloys.

Material	Hf	Nb	Ta	Ti.	Zr	C	N	O	Reference
HfNbTaTiZr	20.1	20.0	20.0	20.1	19.3	0.07	0.10	0.27	[13]
	±0.1	±0.1	±0.1	±0.1	±0.2	±0.01	±0.02	±0.03	
HfNbTaTiZr-3 %O	19.2	19.6	19.4	19.3	19.2	< 0.08	0.03	3.24	This study
	±0.1	±0.1	±0.1	±0.1	±0.2		±0.01	±0.02	

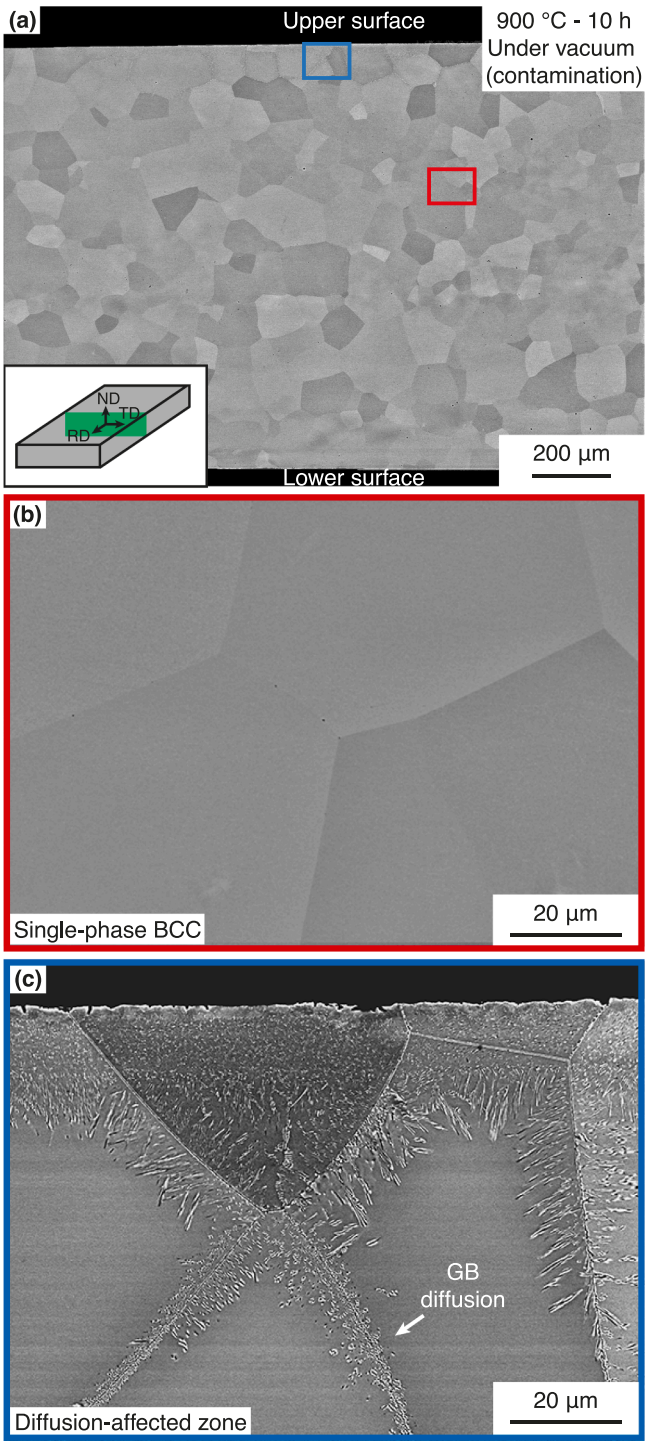

Fig. 1. Microstructure of the HfNbTaTiZr HEA after aging at 900 °C for 10 h under vacuum. (a) Through-thickness cross section of a sheet where its surfaces are visible at the top and bottom of the BSE image. (b) and (c) High-magnification BSE micrographs from the center and edge of the sheet, respectively, see red and blue frames in (a). Heterogeneous precipitation was found to occur at the sample surface where a contamination from the atmosphere occurred.

suspension (MasterMet2 by Buehler, particle size ~0.02 µm, pH ~10) with a ratio of 3:1, respectively. The microstructural evolution upon annealing was investigated with backscattered electron (BSE) micrographs acquired at acceleration voltages ranging from 15 to 30 kV using a JEOL JSM-7200F field emission scanning electron microscope (SEM). This microscope is equipped with an Oxford X-Max 80 SSD EDS spectrometer with which point and line scan analyses were performed to determine the compositions of the different phases. The crystallographic structures of the latter were obtained by EBSD at 30 kV with a probe current of 7 nA and a step size of 0.1 µm. The crystallographic analyses were carried out using the Matlab toolbox MTEX [33] and the grain segmentation was performed using a threshold angle of 10 ° Note that identical results were obtained with an angle of 2 °, indicating that this parameter is not critical for the analyses.

2.3. Elastic strain energy density calculations

To evalutate the morphology and the main growth direction of the HCP precipitates colonies, calculations were performed by considering the elastic energy density e_{el} of laminates composed of the HCP and BCC phases. For this simplified morphology, strain and stress are homogeneous in each phase so that the elastic energy is obtained by solving a linear system in which the components of strain in both phases are the only unknowns. It has been shown that this elastic energy density is the lowest bound of the elastic kernel (independent of the precipitate shape) for a vanishing volume fraction of the product phase (in our case, we have taken $f_{HCP} = 10^{-6}$) [34]. It has been shown in Refs. [35,36] that the shape of the polar representation of e_{el} can be used to predict the shape and growth direction of acicular precipitates in accordance with phase field calculations. The input parameters are the elastic constants and the eigenstrain relating HCP and BCC phases. In a first step, the elastic constants are assumed to be homogeneous and isotropic, corresponding to the BCC polycrystal as determined in Refs. [11,13] ($C_{11} = 95.3$ and $C_{12} = 33.5$ in GPa at 900 °C). As will be shown in Section 3.5, we found the Burgers OR between HCP and BCC in most of the colonies analyzed. For this latter OR, the distortion matrix $\boldsymbol{B}$ transforming BCC into HCP (the shuffle of $\{0002\}_{HCP}$ planes does not contribute to the distortion) is diagonal with the following components: $\sqrt{3}a_{HCP}/\sqrt{2}a_{BCC}$, a_{HCP}/a_{BCC} and $c_{HCP}/\sqrt{2}a_{BCC}$ in the orthogonal frame associated with the $[1\bar{1}0]_{BCC}$, $[001]_{BCC}$, and $[110]_{BCC}$ directions (called ortho-hexagonal frame and noted *oh*). The lattice parameters have been measured by TEM (not shown here) as $a_{BCC} = 3.40$ Å (close to the lattice parameters of pure Ta and Nb) and $a_{HCP} = 3.23$ Å and $c_{HCP} = 5.15$ Å. To fulfill the Burgers OR, a small rotation $\boldsymbol{R}$ of 5.26° around $[110]_{BCC} \,||\, [0001]_{HCP}$ is combined with $\boldsymbol{B}$. The eigenstrain becomes:

$$\varepsilon^* = \begin{pmatrix} 0.194 & 0.01 & 0 \\ 0.01 & -0.025 & 0 \\ 0 & 0 & 0.103 \end{pmatrix}_{oh} \quad (1)$$

In a second step, to investigate the potential effect of elastic anisotropy, the calculations are repeated, assuming that the elastic constants are close to those of Ta in BCC and Zr in HCP. For this purpose, we use the 900 °C data reported for Zr ($C_{11} = 111$, $C_{33} = 141$, $C_{44} = 22.6$, $C_{12} = 83.4$, $C_{13} = 65.6$ in GPa) [37] and for Ta ($C_{11} = 253$, $C_{12} = 143$, $C_{44} = 72$ in GPa) [38].

3. Results and discussion

3.1. Precipitation in the HfNbTaTiZr alloy aged under vacuum

A cross section, spanning the entire thickness of the specimen and illustrated with a green rectangle at the bottom left of Fig. 1a, was investigated after aging the HfNbTaTiZr alloy in an evacuated quartz tube at 900 °C for 10 h. The BSE micrograph in Fig. 1a shows an overview of the microstructure where the upper and lower surfaces of the specimen can be seen at the top and bottom. Regarding the state of these surfaces before aging, it is worth recalling how they were prepared. The cold-rolled specimens were cleaned in ultrasonic baths of distilled water, acetone, and ethanol before being recrystallized at 1373 K for 5 h. During this heat treatment, recrystallization took place, resulting in a clean and non-deformed microstructure with no residual stresses at the

surfaces. Note that the latter were not further prepared before aging, i.e., no cutting, grinding, or polishing were involved. In Fig. 1a, grains with different orientations can be distinguished and no precipitates are detected. A high-magnification BSE image, which was taken from the center of the sheet (see red frame in Fig. 1a), is magnified in Fig. 1b where a single-phase solid solution is still apparent. However, regions close to the surfaces of the sheet (see blue frame in Fig. 1a that is enlarged in Fig. 1c) reveal the presence of precipitates. This indicates that either some elements from the atmosphere diffused in or elements from the alloy evaporated (diffused out), resulting in a change of the local alloy chemistry in the vicinity of the sample surface, which in turn induced a phase transformation, see Section 3.2 for a detailed phase analysis. In Fig. 1c, fine precipitates within grains are observed down to ~20 μm below the sample surface and coarser precipitates are present along grain boundaries down to ~100 μm. This difference reflects the diffusivities in the bulk and along grain boundaries, i.e., grain boundary diffusion is much faster than bulk diffusion [39,40]. As will be shown later, this inhomogeneity of the precipitation at the surface of the aged sample resulted from the diffusion of O that modified locally the stability of the BCC solid solution and led to the precipitation of secondary phases. The inhomogeneous precipitation observed in Fig. 1c clearly shows the importance of investigating the near-surface microstructure of aged specimens, e.g., such regions are generally removed by grinding and easily overlooked in other studies. Finally, one may argue that the surface roughness, resulting from rolling, could promote O adsorption at the sample surface during aging. However, since O adsorption and O diffusion in the material operate in series and the latter is the rate-limiting step [39], the surface roughness is unlikely to affect the precipitation kinetics.

A longer heat treatment at 900 °C for 1000 h was then performed to evaluate its impact on precipitation. The microstructure in Fig. 2a displays precipitates that are mostly present at grain boundaries throughout the entire thickness of the specimen. Here, the red rectangle marks a region in the center of the sheet from where a high-magnification BSE image was recorded (inset of Fig. 2a). The corresponding microstructure reveals coarser precipitates than after the 10-h heat treatment, with darker and brighter contrasts compared to the matrix and sharp interfaces in between, suggesting that two phases have formed. From the same region as the one displayed in the inset of Fig. 2a, an EBSD analysis revealed that the dark precipitates have an HCP crystallographic structure, while the bright precipitates and the gray matrix are BCC. Additional TEM investigations in Figs. S1a-b further showed that these phases do not exhibit superlattice reflections, indicating the absence of long-range order, and that the two BCC phases have different lattice parameters. Based on these analyses, the BSE image in Fig. 2a was segmented using a thresholding method to generate the phase map displayed in Fig. 2b, where the HCP, BCC_2, and BCC_1 phases appear green, blue, and red, respectively. In the high-magnification BSE micrograph in Fig. 2c, dark nano-sized particles can be observed on top of the brighter phases. These are artifacts, resulting from the sample preparation, i.e., silica particles that were involved during polishing with the Vibromet, see Section 2.2.

To investigate the chemical partitioning between the three phases (HCP, BCC_2, and BCC_1), an EDS line scan was recorded along the yellow arrow in Fig. 2c. The corresponding concentration profile is shown in Fig. 2d, where the colored background highlights the three phases. The matrix (BCC_1, red region) is found to be almost equiatomic while the HCP phase (green region) is Hf-Zr-rich and the BCC_2-phase is Ta-Nb-rich (blue region in Fig. 2d). The continuous transitions in the concentration profiles are related to the extended probe size of EDS, which is in the μm range. According to the BSE micrographs and EBSD results, the phase boundaries can be considered as practically sharp. Also shown in Fig. 2e is a qualitative O concentration profile from the same dataset. Note that O cannot be accurately quantified by EDS and that it is difficult to distinguish from N.[1] However, APT analyses on this alloy (not shown here) revealed a negligible N content, consistent with Ref. [41]. Therefore, we only consider the impact of O on phase stability in the following. In Fig. 2e, O is found to preferentially partition to the HCP phase. Based on the results that will be shown later, we conclude that interstitial contamination occurred during annealing, and the contaminants diffused from the surface preferentially along grain boundaries that act as fast diffusion pathways. As O is a well-known HCP stabilizer [42], it probably destabilized the BCC solid solution and triggered the phase transformation ($BCC_1 \rightarrow BCC_2 + HCP$) in the vicinity of grain boundaries.

3.2. *Effect of annealing conditions and O concentration on phase stability*

To prove that the phase decomposition observed in HfNbTaTiZr alloy (see Figs. 1 and 2) was promoted by O contamination, additional heat treatments were performed at 900 °C for 1000 h. First, a sample from the same HfNbTaTiZr alloy was wrapped in a Ta foil[2] and sealed in a quartz tube filled with Ar (~300 mbar) to investigate how the annealing conditions affect phase stability (note that this heat treatment was reproduced twice and led to identical results). Second, the HfNbTaTiZr alloy enriched with ~3 at.% O was annealed under the same conditions to uncover the influence of O on precipitation.

Compared to the HfNbTaTiZr alloy that was contaminated by interstitials during aging under vacuum (Fig. 3a), the same alloy annealed under Ar atmosphere was found to remain single-phase BCC even after 1000 h at 900 °C (Fig. 3b), i.e., the entire cross section of the sample remained free of precipitates. This indicates that the BCC solid solution of the contamination-free HfNbTaTiZr HEA is stable at 900 °C (Fig. 3b) and that the precipitates observed in Fig. 3a were formed during aging due to ongoing interstitial contamination. This further emphasizes the importance of the annealing atmosphere, especially for long heat treatments.

To assess the role of O in the phase decomposition, the O-doped HEA was aged under the same conditions. The corresponding microstructure, depicted in Fig. 3c, is composed of the same phases as in the vacuum aged sample with the formation of HCP and BCC_2 precipitates in the BCC_1 matrix, see Fig. 4. However, differences between the aged microstructures of the O-doped and O-contaminated HEAs are worth mentioning. First, the amounts of HCP and BCC_2 phases are greater in the O-doped HEA than in the O-contaminated alloy, i.e., the volume percentages in HCP and BCC_2 phases (converted from areal fraction assuming isotropy and isometry) in the HfNbTaTiZr-3 %O HEA are 15 and 35 vol.% while they are 6 and 11 vol.% in the O-contaminated HEA, respectively, compare Figs. 2 and 4. Second, although the HCP and BCC_2 precipitates are mostly located at grain boundaries (Fig. 3a) in the O-contaminated alloy, they are more homogeneously distributed in the HfNbTaTiZr-3 %O HEA (Fig. 3c). This difference can be ascribed to the way interstitials were introduced into each alloy, i.e., O diffused from the atmosphere along the grain boundaries and cause a local phase transformation in the contaminated HEA, whereas the presence of ~3 at.

[1] As the peaks of O-K and N-K are very close in EDS spectra, we cannot conclude whether O, N or a combination of both is present in the different phases. Furthermore, in alloys containing substantial amounts of Ti, Ti-L is superimposed to the N-K within relevant energy resolutions of modern EDS detectors.

[2] Ta was chosen to wrap the specimens because it has the highest melting point and the interdiffusion between the foil and the sample is slow enough to prevent the specimen from sticking to the foil.

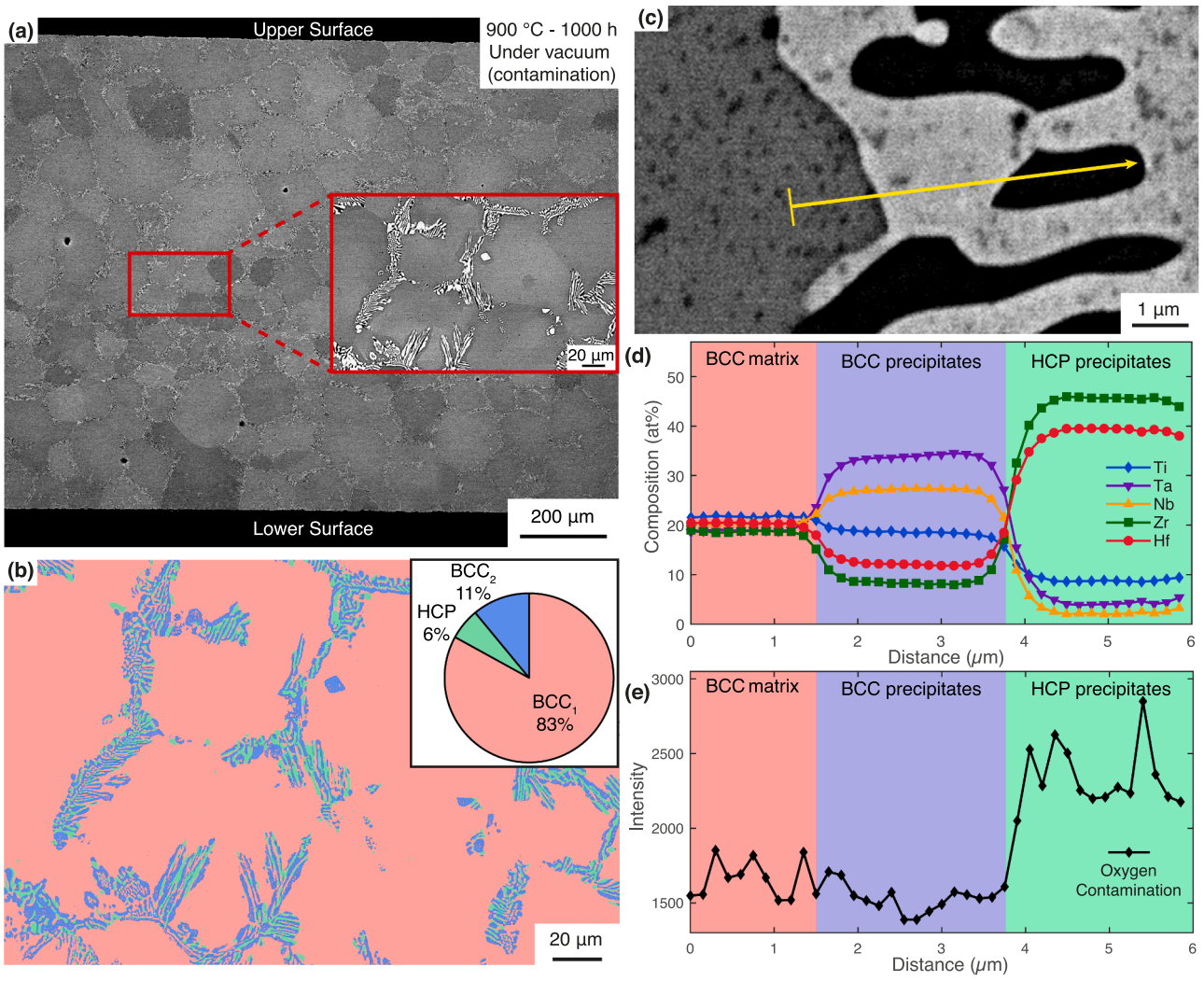

Fig. 2. Decomposition triggered by O contamination from the atmosphere of the initially single-phase BCC HfNbTaTiZr alloy after aging at 900 °C for 1000 h under vacuum. (a) BSE micrograph through the whole thickness of the annealed sheet. Here, the red framed zone was magnified in the inset. (b) Phase map from the same region as that displayed in the inset of (a). The phase fractions of the matrix (BCC_1, light red) and precipitates (BCC_2: light blue, HCP: light green) are represented in the pie chart. (c) High-magnification BSE image where the yellow line indicates the region from where the EDS line scan in (d) was recorded. (e) Oxygen intensity along the line scan showing preferential partitioning to the HCP phase.

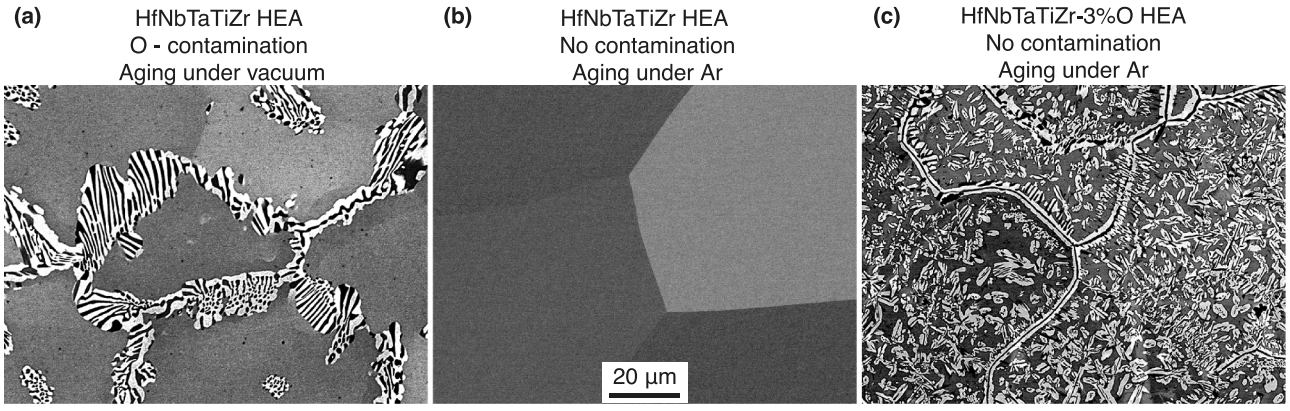

Fig. 3. Comparison of the microstructures of the three HfNbTaTiZr HEAs aged at 900 °C for 1000 h. (a) Alloy aged under vacuum and experiencing O contamination upon annealing. (b) Alloy aged under Ar without any contamination. (c) HfNbTaTiZr-3 %O alloy that was aged under Ar. All BSE images were taken in the center of the specimen for comparison purposes.

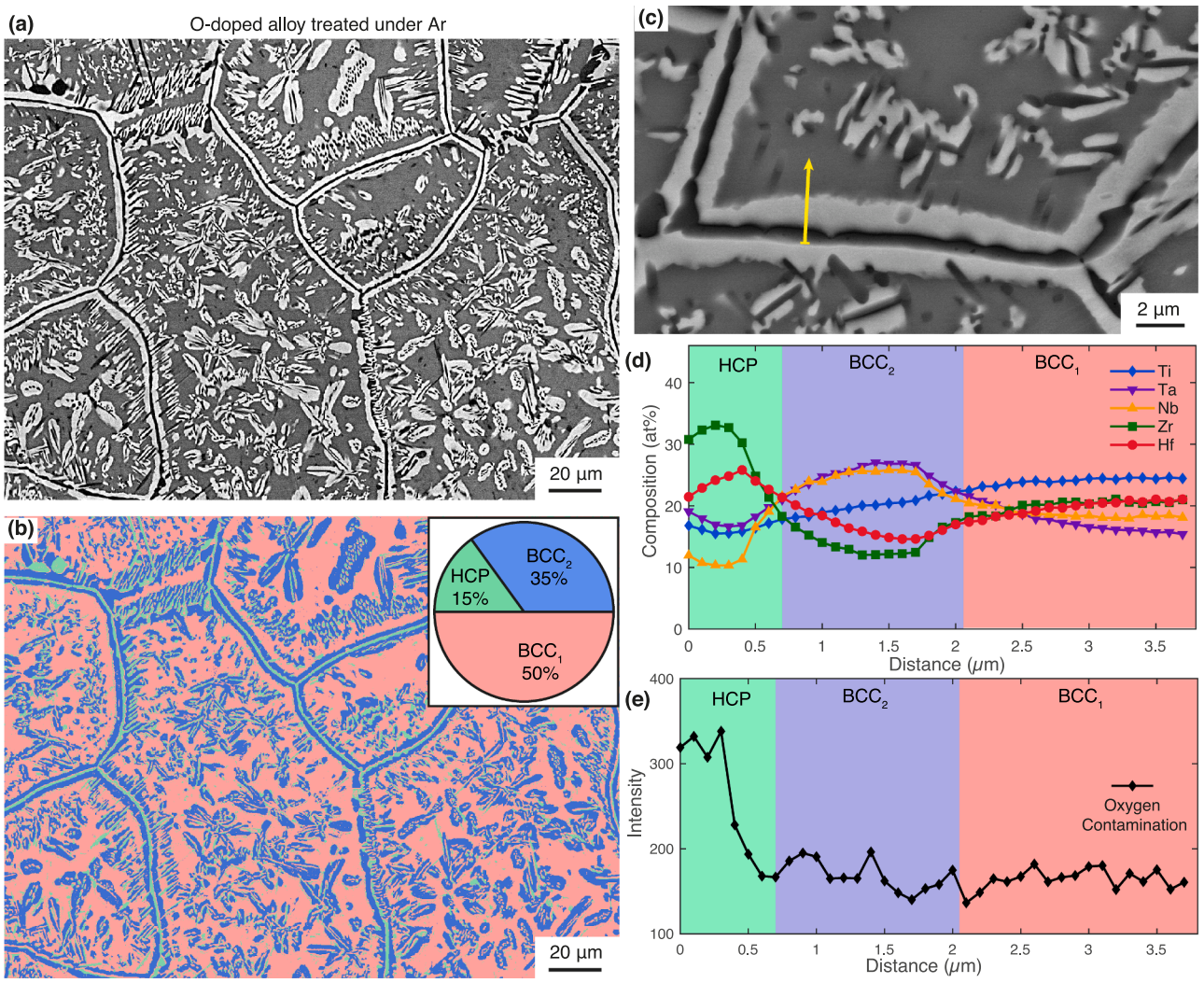

Fig. 4. Phase separation in the initially single-phase BCC HfNbTaTiZr-3 %O that was aged at 900 °C for 1000 h under Ar. (a) BSE micrograph taken far away from the sample surface revealing the presence of three phases (dark, bright, and gray). (b) Phase map from the same region as in (a). The surface area fractions of the matrix (BCC_1, light red) and two types of precipitates (BCC_2: light blue and HCP: light green) are provided in the pie chart in the upper right corner of (b). (c) BSE micrograph where the yellow arrow marks the line along which the EDS line scan shown in (d) was recorded. Here, note that the electron penetration depth (~1 µm) is slightly larger than the typical sizes of the different phases. Therefore, the phase compositions are only qualitative. (e) O-intensity profile along the yellow arrow in (d).

% O in the doped HEA induced a more homogeneous precipitation with the presence of secondary phases not only at grain boundaries but also within grains. Third, in the O-doped alloy, precipitates are finer, and their number density is much higher than in the O-contaminated alloy. This may reflect the fact that the interstitial concentration is larger in the former alloy.

3.3. Possible precipitation pathways

We have previously shown that the equiatomic HfNbTaTiZr alloy with a low O concentration of ~0.3 at.% forms a stable single-phase BCC solid solution at 900 °C, see Fig. 3b. However, the stability of the BCC phase is shifted by O contamination (Fig. 3a) or O doping (Fig. 3c), which induces the heterogeneous formation of lamellae consisting of two phases, i.e., a Zr-Hf-O-rich HCP phase (dark contrast in BSE) and a NbTa-rich BCC_2 phase (bright contrast in BSE, Fig. 3a,c). The lamellar structures resemble those typically observed due to either discontinuous precipitation or a monotectoid reaction, both of which can be described by the reaction $BCC_1 \rightleftharpoons HCP + BCC_2$ [43]. To identify the type of reaction occurring in Figs. 3a,c, we used the classification of solid-state, heterogeneous phase transitions reported in the review article of Manna et al. [44]. Based on the results presented in Figs. 2d and 4d, since the HCP and BCC_2 phases have different compositions compared to the matrix, their formation requires long-range diffusion, and the transformation is therefore diffusive. As shown in Fig. S1 (and in Section 3.4), the newly formed BCC_2 phase displays the same crystallographic orientation as the BCC_1 phase. This result contradicts the reaction sequence of a discontinuous precipitation as a combined recrystallization and precipitation process, i.e., a sharp change in crystal orientation between the BCC_1 and BCC_2 phases across the reaction front would be expected for a discontinuous precipitation [44,45]. Therefore, it can be concluded that the $BCC_1 \rightleftharpoons HCP + BCC_2$ transformation, which is induced by O contamination or O doping, corresponds to a monotectoid reaction, implying the existence of a BCC miscibility gap in the Hf-Nb-Ta-Ti-Zr system. This hypothesis is supported by the fact that such a monotectoid transformation exists or is speculated for several binary phase diagrams of the Hf-Nb-Ta-Ti-Zr system, e.g., Hf-Ta [46], Nb-Zr [47], and Ta-Zr [48].

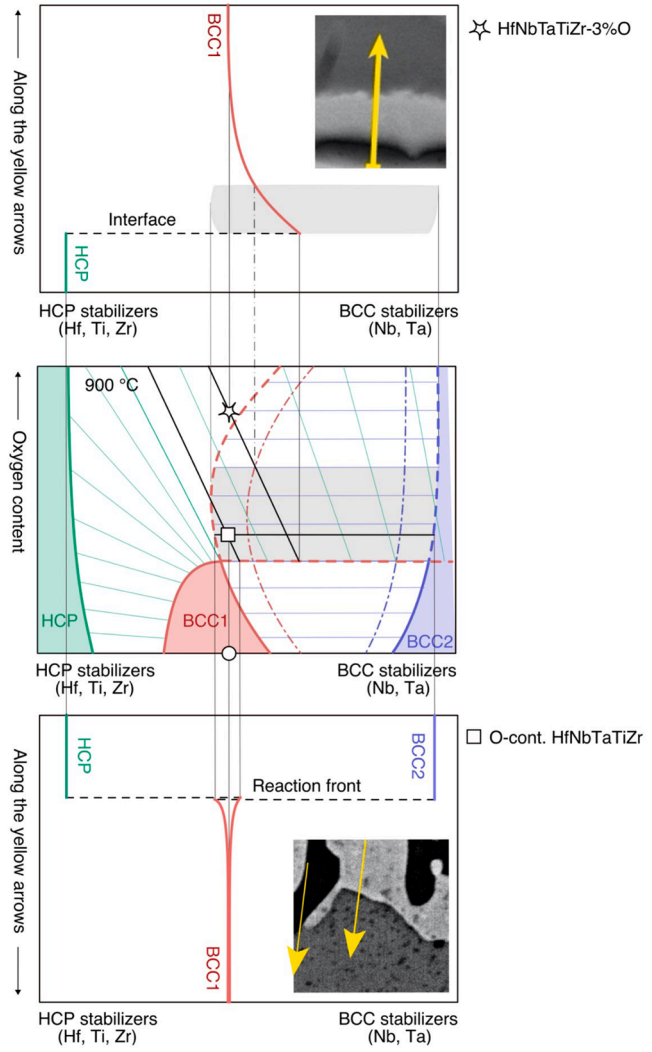

Fig. 5. (Center of the image) Qualitative ternary isothermal section at 900 °C of the Hf-Nb-Ta-Ti-Zr-O alloy system with substitutional BCC and HCP stabilizers on the left and right sides of the horizontal axis and O on the vertical axis, showing the two-phase fields HCP + BCC_1 (green tie lines) and BCC_1 + BCC_2 (blue tie lines). The alloys investigated in the present work at 900 °C are highlighted with symbols: HfNbTaTiZr without (white circle) and with O contamination (white square), HfNbTaTiZr-3 %O (white star). (Top) Schematic concentration profiles along the yellow arrow during the growth process in O-enriched alloy (the gray area indicates the region where a spinodal decomposition occurs). (Bottom) Schematic concentration profiles along the yellow arrows during the coupled growth process in the O-contaminated alloy.

An interpretation of the role of O contamination and O doping on the $BCC_1 \rightleftharpoons$ HCP + BCC_2 transformation is proposed based on the qualitative pseudo-ternary[3] isothermal section at 900 °C in the center of Fig. 5. Note that this isothermal section, which incremental construction is detailed in section B of supplementary materials, represents a portion of a right-angled triangle for low O concentrations up to ~4 at.%, i.e., the right angle is located at the bottom left and a part of the hypotenuse of the triangle is represented by the edge between the very thin white region at the top right of the isothermal section and the blue area. Although partly hypothetical, this section combines qualitatively different features of available binary [49-51] and ternary diagrams. Hf promotes the stability of HCP in the rich (Hf, Ti, Zr) corner and a miscibility gap lies in the BCC phase field following the binary diagrams Hf-Nb, Hf-Ta, Zr-Nb and Zr-Ta. The extensions of the HCP and BCC phase fields with O are inspired by the isothermal sections Zr-Nb-O at 100 °C [52] and Ti-Nb-O at 800 °C [53]. The stable pseudo-ternary diagram[4] is given in Fig. S2 of supplementary materials: the alloys containing some O are located in the three-phase field HCP + BCC_1 + BCC_2 in agreement with the experiments. Only the two-phase fields HCP + BCC_1 and BCC_1 + BCC_2 (miscibility gap) are plotted in the center of Fig. 5, with the metastable parts plotted with dashed lines (hidden by the three-phase field HCP + BCC_1 + BCC_2 and the two-phase field HCP + BCC_2 in the stable diagram in Fig. S2). In the center of Fig. 5, tie lines are also drawn in these two-phase fields (thin green lines for HCP + BCC_1 and thin blue lines for BCC_1 + BCC_2) for supporting the explanations, although the real tie lines of the full quinary alloy with O will not lie in the same ternary section. Hence, where the green tie lines are drawn, HCP is in equilibrium (stable or metastable) with BCC_1; where the blue tie lines are drawn, BCC_1 is in equilibrium with BCC_2. In between the dashed-dotted lines corresponding to the spinodal, the BCC phase is unstable and decomposes into BCC_1 + BCC_2 by a spinodal decomposition process.

Table 2
Diffusivities (D) and typical time (t) required for the elements to diffuse through a 1 nm thick interface in the Hf-Nb-Ta-Ti-Zr system at 900 °C. The diffusivities from Ref. [21] were extrapolated to 900 °C using an Arrhenius law to calculate the diffusion time t = 1/(4D) with D in nm^2/s [40].

	Hf	Nb	Ta	Ti	Zr
D (nm^2/s)	20,191	681	2	1079	541
t (s)	1.2×10^{-5}	3.7×10^{-4}	1.25×10^{-2}	2.3×10^{-4}	4.6×10^{-4}

The use of this diagram to explain the different microstructures as a function of O content is based on the common hypothesis that the interfaces are in local equilibrium. Their concentrations are given by the tie lines connecting the single-phase fields. To support this assumption, we have calculated the time required for the species to diffuse over a distance typical of interface thicknesses (1 nm) in Table 2. 2. Even for the slowest species, Ta, this time is much less than the duration of aging, so we can reasonably expect the interfaces to be in local equilibrium.

At 900 °C, the HfNbTaTiZr alloy is single-phase BCC, as represented by the white circle in the red BCC_1 region in Fig. 5 (center). When O contamination occurs, the O distribution becomes inhomogeneous, i.e., the local O concentration is higher at grain boundaries (GBs) and lower within grains with a concentration gradient in between. Since O is a strong HCP stabilizer, the vicinity of GBs enters the metastable two-phase field HCP + BCC_2, represented by the white square in the ternary section in Fig. 5. Moreover, it is likely to be located within the metastable miscibility gap (to the right of the BCC_1/BCC_2 boundary, represented by the curved red dashed line), but outside the unstable region delimited by the BCC spinodal (to the left of the red dashed-dotted line). Hence, the regions near the GBs are in the region where monotectoid cooperative growth of HCP and BCC_2 in BCC_1 is possible. Assuming that the interfaces are at local equilibrium, the corresponding schematic concentration profiles of HCP and BCC stabilizers are drawn for neighboring HCP and BCC_2 regions along the yellow arrows in the inset micrograph (bottom of Fig. 5), using the metastable equilibrium tie lines passing through the white square (center of Fig. 5). It must be emphasized again that the tie lines are only illustrative and that the

[3] The substitutional HCP stabilizers, e.g. Hf, Ti and Zr on one hand, and the BCC stabilizers, e.g. Nb and Ta, on the other hand are gathered to pseudo components.

[4] To evaluate the correctness of our qualitative equilibrium diagram, a section of the pseudo-ternary $(TiZrHf)_{1-2x}(NbTa)_{2x}O$ diagram was calculated using ThermoCalc and the TCNI8 database. The two diagrams in Figs. S2 and S3 are similar, but since the database was not optimized for the Ti-Zr-Nb-Hf-Ta-O system, these ThermoCalc calculations remain only qualitative.

actual operative tie lines may differ from those passing through the "nominal" compositions if the diffusivities of the species are different [54]. The growth of the monotectoid colonies is also controlled by O availability and stops when almost all the oxygen has been incorporated into the HCP phase (the process is not illustrated in Fig. 5 because it involves a complex construction that considers the evolving heterogeneity of O between the GBs and the grain interiors).

The grain boundaries of the aged HfNbTaTiZr-3 %O alloy were found to be systematically covered by a continuous layer of HCP phase (see Figs. 3c, 4a,c), thus indicating that HCP precipitation proceeds first. The representative composition (white star in the center of Fig. 5) is likely to be also in the metastable HCP + BCC_1 two-phase field, but outside of the metastable BCC_1 + BCC_2 miscibility gap (to the left of the red dashed line). The HCP precipitates (at the grain boundary as well as in the interior of the grains) grow and reject the BCC stabilizers, as illustrated with the concentration profile at the top of Fig. 5. When the BCC_1 side of the interfacial tie line enters the unstable region in the miscibility gap at some step of the process, the BCC_1 regions surrounding the HCP precipitates undergo some spinodal decomposition, as illustrated by the gray-shaded region in Fig. 5. This is consistent with HCP always being surrounded by BCC_2, which is rich in BCC stabilizers.

As an alternative precipitation pathway (not illustrated in Fig. 5), if the BCC_1 side of the interfacial tie line does not enter the unstable region but remains in the miscibility gap so that there would be some driving force for BCC_2 precipitation, BCC_2 could nucleate at the HCP/BCC_1 interface (again, assumed to be at local equilibrium) and grow in a proportion allowed by the supersaturation of the surrounding regions in BCC stabilizers.

The scenarios described above and relying on the strong influence of O on the structure of the phase diagram are consistent with all the observations and concentration measurements.

3.4. Precipitation at grain boundaries and special boundaries (coincidence site lattice)

A comprehensive study of the precipitation process occurring in the O-contaminated alloy was carried out using the grain orientation map shown in Fig. 6a, which covers 19 grains of the BCC_1 matrix numbered from 0 to 18. Here, the HCP precipitates appear as small dots or needles while the BCC_2 precipitates cannot be distinguished from the BCC_1 matrix since both phases have the same crystal structure and orientation within a given grain. While the HCP precipitates are generally found to nucleate at GBs and to grow towards the core of the grains, some GB regions remain devoid of HCP precipitates, e.g., parts of the boundaries between grains 0 and 1, 1 and 6, 4 and 5, 11 and 13, 11 and 12, 12 and 15, 14 and 15, see Fig. 6a and Table 3. To evaluate whether these interfaces correspond to special GBs, such as coincidence-site-lattice (CSL) boundaries, the following protocol was applied. From the EBSD map in Fig. 6a, the misorientation angle and the rotation axis between neighboring grains were obtained. Both data were then compared to the list of misorientation angles and rotation axes for CSL boundaries in BCC structures reported by Warrington and Bufalini [55] and provided in Table S1 of Supplementary Materials, which allowed to identify CSL boundaries. As examples, the schematic unit cell of each grain in Fig. 6b and c is shown in red, the projections of the rotation axes are represented by short black lines intersecting the boundary, whereas the color of the boundary represents the misorientation angle. At the 11/12 boundary in Fig. 6b, the rotation axis is ⟨322⟩ and the misorientation angle is 46.3°, equivalent to 180° – 46.3° = 133.7° According to the table provided by Warrington and Bufalini [55], a boundary with a 133.7° misorientation angle and a ⟨332⟩ rotation axis corresponds to a Σ11 [332]-CSL boundary[5] [56]. As another example, the 11/13 boundary in Fig. 6c is found to have a ⟨331⟩ rotation axis with a 51.6 ° misorientation angle, corresponding to a Σ25 [331]-CSL boundary.

A systematic analysis was conducted on each precipitate-free boundary (PFB) to assess if they correspond to CSL boundaries. These analyses, provided in Fig. S4 and summarized in Table 3, revealed that most PFB are CSL boundaries. Besides, no preferential CSL was evidenced, i.e., all of them were different in our data set.

To assess the prevalence of CSL boundaries in the microstructure, their length fraction, defined as the ratio of their length to the total length of the boundaries, was measured to be 14 %. This shows that ~86 % of the grain boundaries undergo a phase transformation due to oxygen diffusion during the aging process.

3.5. Orientation relationships between the different phases

A complementary study was carried out to identify the ORs between the different phases. A comparison of the low-magnification and high-magnification BSE images in Fig. 7a,c and the corresponding grain orientation maps in Fig. 7b,d, respectively, reveals that the bright BCC_2 phase in Fig. 7a,c cannot be distinguished from the matrix in Fig. 7b,d. This suggests that the BCC_2 phase has the same crystal structure and orientation as the matrix with a cube-on-cube OR but a different composition, see Fig. 2d.

In the following, we investigate the ORs between BCC phases and colonies of HCP precipitates with the same orientation. 27 colonies were analyzed and their locations and designations are given in Fig. S5. As an example in Fig. 7d, the unit cells of the HCP precipitates in colony 6d and the BCC phases in grain 6 are shown in green and red, respectively. From the stereographic projections of both structures that are depicted in Fig. 7e, the following OR can be deduced: $(110)_{BCC}$ || $(0001)_{HCP}$ and $[1\bar{1}1]_{BCC}$ || $[11\bar{2}0]_{HCP}$, which corresponds to the Burgers OR (BOR) and is most commonly observed between BCC and HCP structures in Ti and Zr alloys [31,57,58]. Using the same procedure, the other 26 colonies were analyzed to determine their ORs with the surrounding BCC phases and the results are summarized in Table 4.

Most colonies of HCP precipitates exhibit the BOR with the BCC phases (20 colonies out of 27). However, six colonies were found to show a near BOR $(\bar{1}10)_{BCC}$ || $(\bar{1}011)_{HCP}$ and $[113]_{BCC}$ || $[11\bar{2}3]_{HCP}$ as predicted by Zhang and Kelly [59] using an edge-to-edge matching crystallographic model. Besides, the Rong-Dunlop OR with $(021)_{BCC}$ || $(0001)_{HCP}$ and $[100]_{BCC}$ || $[2\bar{1}\bar{1}0]_{HCP}$ [60] was verified in one colony. These results confirm that the majority of colonies obey the BOR and reveal that other ORs can also occur. According to Zhang and Kelly [59], the presence of these ORs results from the lattice parameter ratios c_{HCP}/a_{HCP} and a_{HCP}/a_{BCC}: while the BOR is promoted in all cases, the OR $(\bar{1}10)_{BCC}$ || $(\bar{1}011)_{HCP}$ and $[113]_{BCC}$ || $[11\bar{2}3]_{HCP}$ is favored for an a_{HCP}/a_{BCC} ratio around 0.9–1.0 and a c_{HCP}/a_{HCP} ratio around 1.5–1.6. In the HfNbTaTiZr alloy aged at 900 °C under vacuum, the a_{HCP}/a_{BCC} and c_{HCP}/a_{HCP} ratios are ~0.97 and ~1.56, respectively. These results are consistent with the requirements proposed by Zhang and Kelly.

The same orientation analysis was performed in the HfNbTaTiZr-3 % O alloy on 24 precipitate colonies (see Fig. S6). As for the O-contaminated alloy, the majority of the colonies showed the BOR with the adjacent BCC phase (22 out of 24), while the Zhang-Kelly OR was evidenced in two colonies (details are provided in Supplementary Materials).

3.6. Morphologies of the HCP precipitates and their preferential growth direction

Precipitation of the HCP phase occurred heterogeneously at grain boundaries of the BCC matrix during annealing of the O-contaminated HfNbTaTiZr HEA and hence could either take place on static or moving GBs. It seems, from Fig. 6a, that precipitates growing on migrating GBs do not have a particular growth direction and are more or less wavy, as

[5] This notation indicates that both grains are related by a rotation around the [332] axis and Σ is the reciprocal density of coincidence sites.

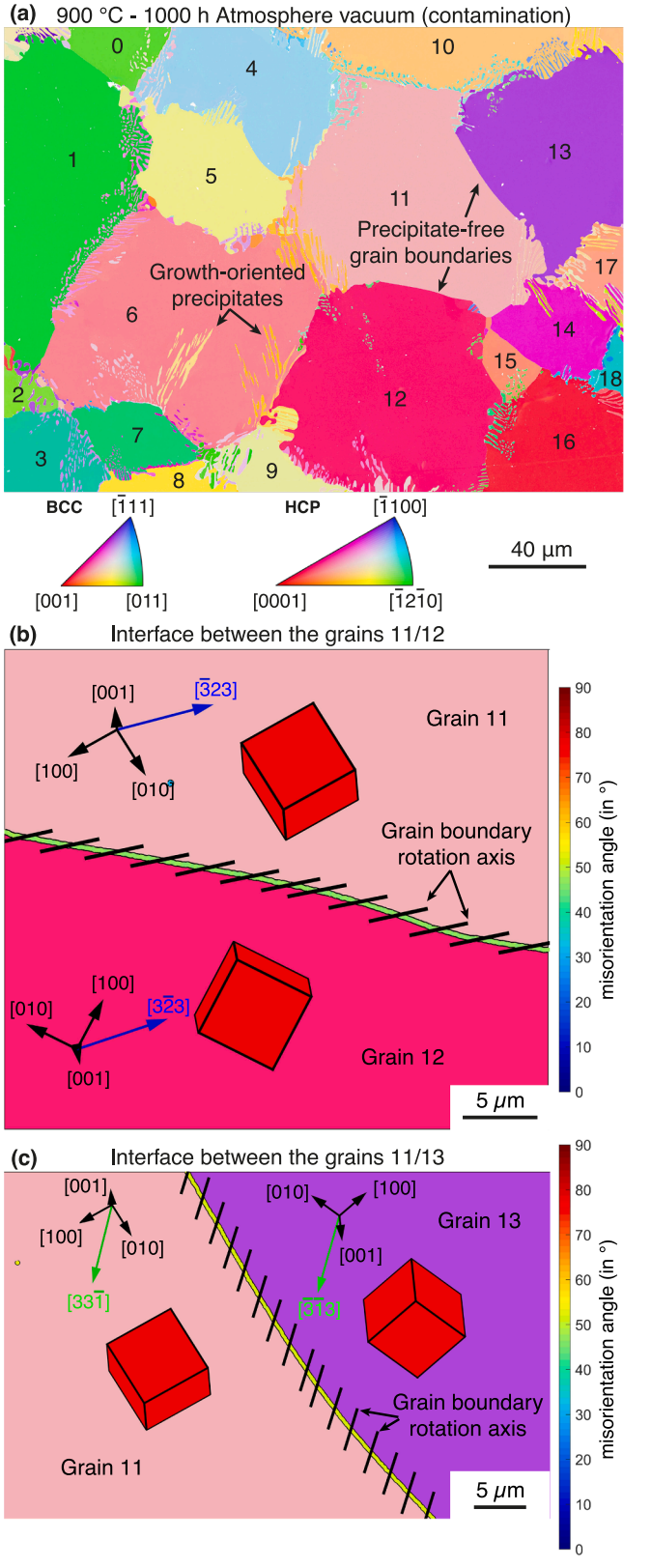

(caption on next column)

Fig. 6. Crystallographic analyses in the HfNbTaTiZr HEA that was contaminated by O during aging in vacuum at 900 °C for 1000 h. (a-c) Color-coded grain orientation maps obtained by EBSD where the colors indicate the crystal orientations parallel to the direction normal to the image, see stereographic triangles of the HCP and the BCC phases at the bottom of (a) for color decoding. In (a), all grains are numbered to ease the identification of the grain boundaries. (b,c) Magnified grain boundaries devoid of precipitates between grains (b) 11 and 12 and (c) 11 and 13. In each grain, the BCC unit cell is illustrated by a red cube, and the ⟨100⟩ vectors are represented. The misorientation angle between grains is indicated by the color of the boundary (see corresponding scale on the right of (b,c)) and the projection of the grain boundary rotation axis is represented by short black lines that intersect the boundary. The common direction in both grains is highlighted with blue and green vectors in (b) and (c), respectively.

for example the colonies 1a, 4c, 7a, 9a or 11c (see Fig. S5). In these cases, the precipitation only appear perpendicular to the GB or parallel to the moving direction of the GB. It is also interesting to note that the non-BORs are often found at migrating GBs (e.g., colonies 4a, 4c, 5a, 9a, and 11c) or near triple junctions (e.g., 4b, 9a, 11a, and 11c), thus indicating that their occurrence is probably accidental.

In the case of static GBs, the HCP precipitates appear to present two types of morphology (e.g., Fig. 7b), i.e., rounded or elongated. It is also worth noting that the diameter of the rounded precipitates is nearly the same as the thickness of the elongated ones. Considering that these morphologies may result from the metallographic section of the 3-dimensional precipitates, it is reasonable to assume that the precipitates have a rod-like shape. To study their growth directions, we performed a trace analysis of the elongated precipitates in several colonies, as depicted in Figs. 8 and S7. Here, significant deviations of up to ~20° between precipitate directions are observed within the same colonies, e.g., the extreme and average growth directions are represented by blue dashed lines in Figs. 8 and S7. It appears that the average growth direction is comprised between the ⟨100⟩ and ⟨311⟩ directions.

In the HfNbTaTiZr-3 %O alloy, moving GBs were rarely observed (Fig. S6), probably because they are more effectively pinned by a higher number density of precipitates (which formed earlier) compared to the O-contaminated alloy. As a result, accidental non-BORs were less frequently encountered in this alloy. There is a large number density of small HCP precipitates in the interior of the grains in the HfNbTaTiZr-3 %O alloy while the contaminated sample exhibits a very low density of large precipitates at GBs. This may reflect that the undercooling in the contaminated alloy is much smaller than in the doped one. As for the contaminated HfNbTaTiZr alloy, a trace analysis was carried out on four colonies of the O-doped alloy (see Fig. S8). The average growth directions, comprised between the ⟨100⟩ and the ⟨311⟩, are very similar to those evidenced in the contaminated sample. It should though be noted that a much smaller deviation between precipitates growth directions in a given colony is observed in the doped alloy. These results suggest that if O addition plays a major role on phase stability, it only has a minor impact on the growth direction of the precipitates.

To rationalize the morphology and the main growth direction of the HCP precipitates, simple calculations were performed using the method exposed in Section 2.3. In a first step, the elastic energy density e_{el} was computed for all the orientations of an HCP plate with BOR and considering homogeneous and isotropic elastic constants. The resulting 3D polar representation is plotted in the cubic reference frame of the matrix in Fig. 9a. The overall shape resembles almost a cylinder, with shallow minima close to the $\langle 110 \rangle_{BCC}$ direction (light blue). According to Ref. [36], the growth direction corresponds to the maximum e_{el}, i.e., approximately along $\langle 100 \rangle_{BCC}$. The non-circularity within $\{100\}_{BCC}$ is only moderate, indicating in-plane isotropy. Thus, the shape suggested by the elastic energy calculations is close to a rod shape with the longitudinal axis along $\langle 100 \rangle_{BCC}$. This is consistent with the experimental observations.

In a second step, anisotropic elastic constants that are different in the

Table 3
Identification of the type of coincidence-site-lattice (CSL) corresponding to each precipitate-free boundary. For each of them, the misorientation angle and the rotation axis were calculated from the EBSD data. If a match was found between these values and the table reported by Warrington and Bufalini [55], the type of CSL boundary was deduced.

Grain boundary	0/1	1/6	4/5	11/12	11/13	11/14	12/15	14/15
Misorientation angle	17.4 °	57.9 °	47.4 °	46.3 °	51.6 °	50.1 °	39.5 °	16.7 °
Rotation axis	⟨533⟩	⟨111⟩	⟨320⟩	⟨332⟩	⟨331⟩	⟨431⟩	⟨100⟩	⟨120⟩
Type of CSL boundary	Σ11 [533]	Σ3 [111]	6–8° from Σ3 [210]	Σ13 [332]	Σ25 [331]	3° from Σ15 [431]	Σ5 [100]	Σ23 [210]

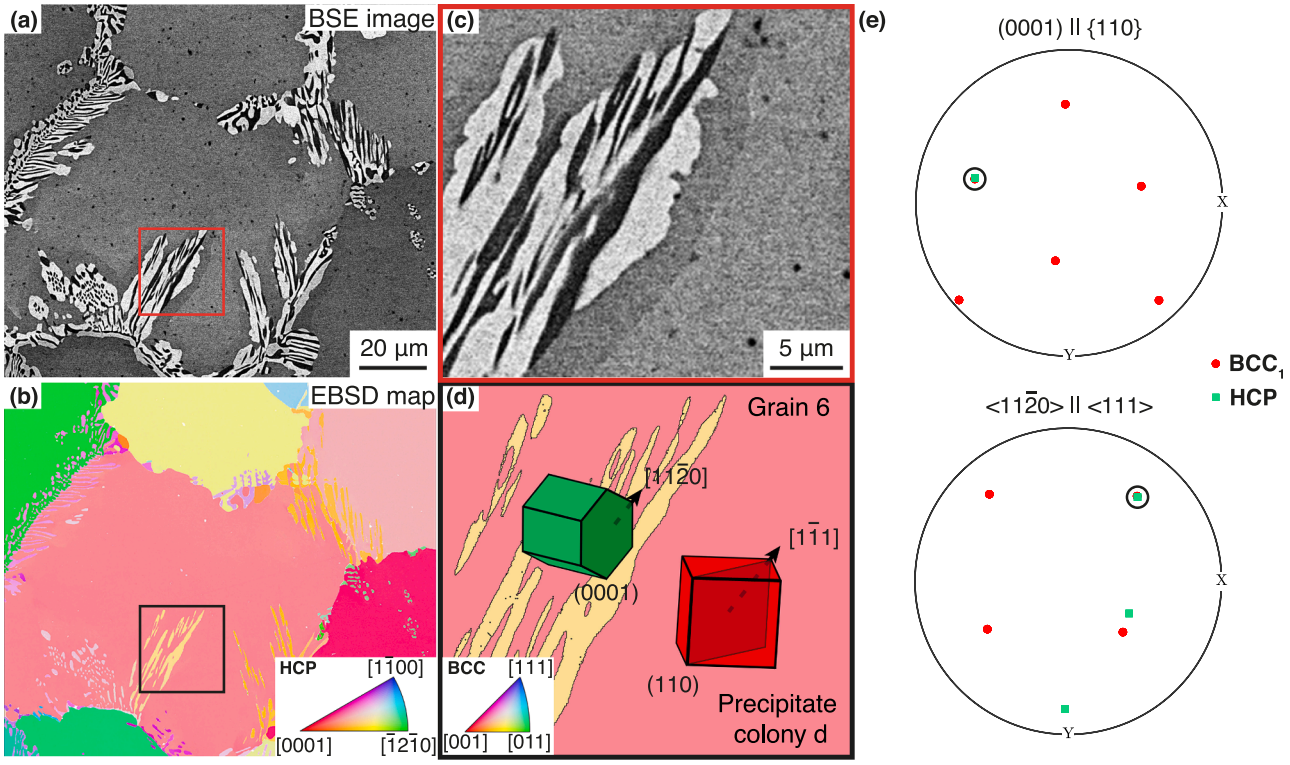

Fig. 7. Determination of the orientation relationship (OR) between the different phases in the HfNbTaTiZr alloy contaminated by O after aging in vacuum at 900 °C for 1000 h. (a) BSE image and (b) EBSD grain orientation map, recorded from the same area. The region framed in red in (a) and in black in (b) are magnified in (c) and (d), respectively. The OR between the BCC phases in grain 6 and the HCP precipitates of colony 6d are shown in (d) where the HCP and BCC unit cells are represented in green and red, respectively. The color codes for the orientations of the HCP and BCC phases are indicated by the stereographic triangles at the bottom of (b) and (d). (e) Superposition of stereographic projections along the (0001) and ⟨11$\bar{2}$0⟩ poles of the HCP precipitates and the {110} and ⟨111⟩ poles of the BCC phases, respectively. The black circles mark the congruent poles of the HCP and BCC structures.

Table 4
Overview of the orientation relationships between BCC phases and 27 colonies of HCP precipitates. Also provided is the proportion of each OR.

BCC/HCP orientation relationships	$(110)_{BCC}$ || $(0001)_{HCP}$ $[1\bar{1}1]_{BCC}$ || $[11\bar{2}0]_{HCP}$	$(021)_{BCC}$ || $(0001)_{HCP}$ $[100]_{BCC}$ || $[2\bar{1}\bar{1}0]_{HCP}$	$(\bar{1}10)_{BCC}$ || $(\bar{1}011)_{HCP}$ $[113]_{BCC}$ || $[11\bar{2}3]_{HCP}$
Proportion of colonies presenting the OR	20/27	1/27	6/27

two phases were considered (listed in Section 2.3). The overall shape of the polar e_{el} plot does not change drastically (Fig. 9b): the maximum remains along $\langle 100\rangle_{BCC}$, the minima become less pronounced, and the section is slightly more elliptical. This last calculation highlights the relevance of the elastic constants, besides the eigenstrain, for the growth direction and shape of the precipitate.

Different reasons can be proposed to explain why the predictions agree only approximately with the observations.

First, it should be emphasized that the input data are approximate, i.e., the HCP and BCC_2 regions are not pure Zr and Ta, respectively, so that their actual elastic constants differ from those chosen for the calculations. More importantly, the lattice parameters entering the eigenstrain are only available with limited experimental precision. They have been measured in a two-phase microstructure, so that they may not be completely relaxed. To illustrate the sensitivity of the shape analysis to the lattice parameters, it can be noted that the expression of the Burgers distortion $\boldsymbol{B}$ is the same for the BCC → HCP transformation of Ti and Zr (and their alloys). However, considering their lattice parameters (e.g., $a_{BCC} = 3.316$ Å, $a_{HCP} = 2.98$ Å, $c_{HCP} = 4.74$ Å for Ti, as deduced from *in-situ* measurements at 900 °C using high energy XRD [61,62]), their eigenstrains feature a large $\langle 1\bar{1}1\rangle_{BCC}$ shear in the $\{110\}_{BCC}$ planes, i.e., with diagonal components about 10 %, −10 % and at most 1 %, in the same ortho-hexagonal frame as for Eq. (1). These values are clearly very

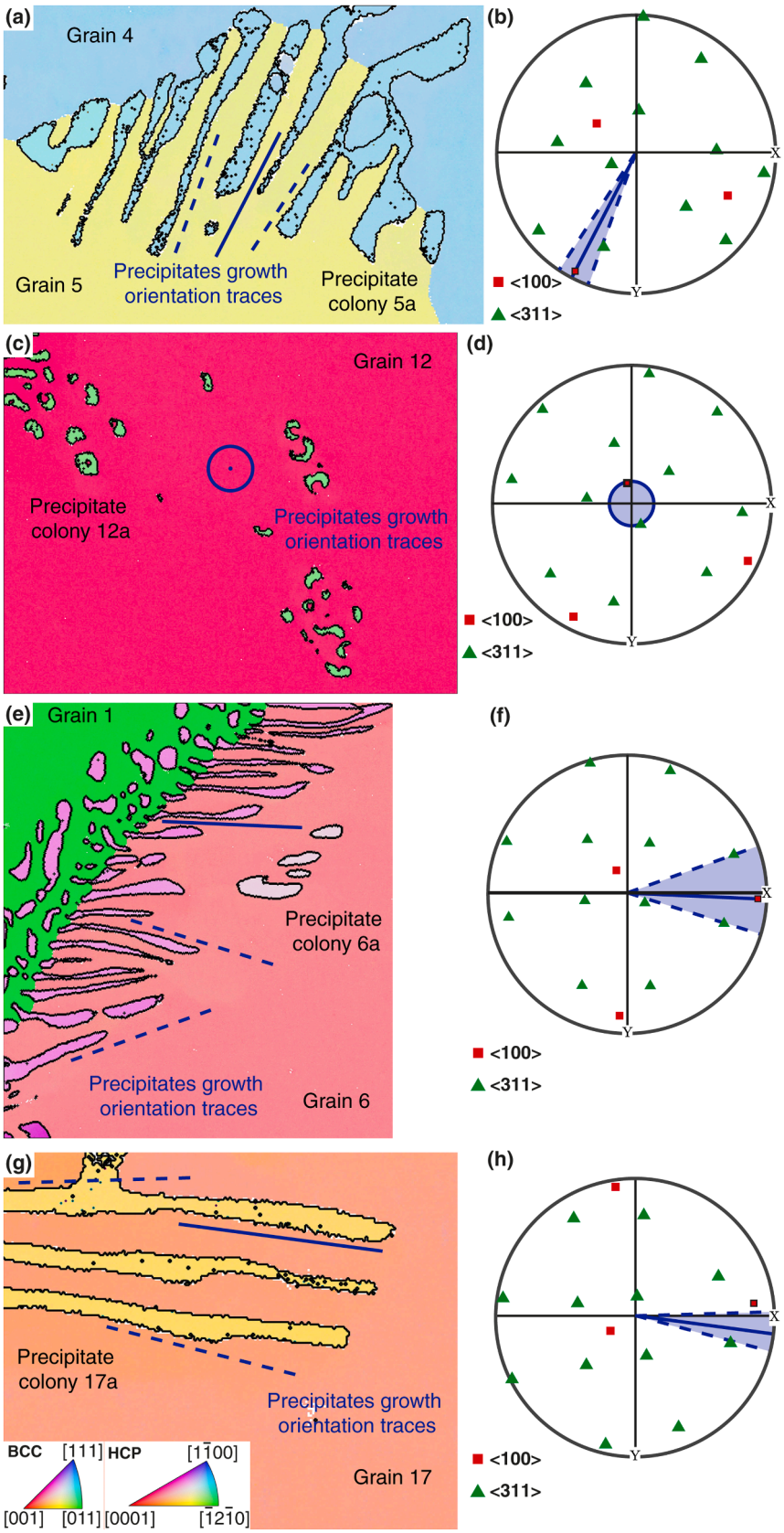

(caption on next page)

Fig. 8. Trace analysis of precipitate colonies to identify their growth directions in the HfNbTaTiZr alloy contaminated by O after aging in vacuum at 900 °C for 1000 h. (a), (c), (e) and (g) EBSD grain orientation maps in the grains 5, 12, 6 and 17, respectively. The color codes for the orientations of the HCP and BCC phases are indicated by the stereographic triangles at the bottom of (g). (b), (d), (f) and (h) Stereographic projections along the ⟨100⟩ (red) and ⟨311⟩ (green) poles of the BCC phases. For each colony, the trace of the average growth orientation is represented by a blue solid line and the two extreme growth directions are represented by blue dashed lines. The blue area in the stereographic projections corresponds to the growth orientation that the precipitates of the corresponding colony can potentially follow.

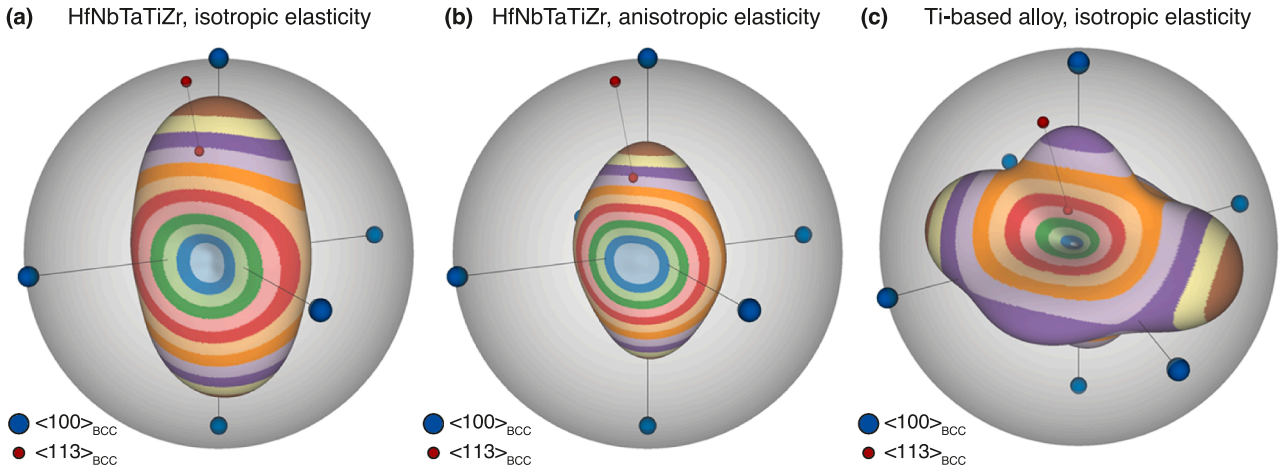

Fig. 9. Polar plots of the elastic kernel e_{el} corresponding to the BCC → HCP transformation in the cubic frame of the BCC lattice considering (a) homogeneous, isotropic elastic constants; (b) inhomogeneous anisotropic elastic constants; (c) the Burgers distortion for Ti (homogeneous isotropic elastic constants). The unit sphere corresponds to 3 kJ/m^3 for (a) and (b) and 0.5 kJ/m^3 for (c). In all plots, the direction with blue dots is $\langle 100\rangle_{BCC}$ and the one with red dots is $\langle 113\rangle_{BCC}$.

different from Eq. (1) and give rise to a very different polar representation, as shown in Fig. 9c: it has been shown in Ref. [35] that this representation corresponds to plates with the short axis parallel to the direction of the deep minima of the polar e_{el} (close to $\{335\}_{BCC}$) and the fastest growth direction along the $\langle 1\bar{1}0\rangle_{BCC}$ direction (brown maximum in Fig. 9c). It is obviously very different from the observation for the present case but consistent with the plate-like morphology of HCP precipitates observed in conventional β-Ti and β-Zr based alloys.

Second, the strain and stress fields are likely to be modified with respect to the simplified calculations by the real microstructural configuration: (i) there are elastic interactions between neighboring precipitates, (ii) even though being very similar, the two bcc phases have different lattice parameters and elastic constants and are separated by an interface that will all together affect elastic energy density.

Finally, it is worth noting that the magnitudes of the predicted elastic energy density in the HfNbTaTiZr HEA are six times greater than for the plates in Ti (and Zr) based alloys. Hence, a significant part of this energy should be relaxed by dislocation activities near the precipitates and/or misfit dislocations so that the growth direction may slightly deviate from the expected $\langle 100\rangle_{BCC}$. Kernel average misorientation (KAM) measurements (not shown here) do not indicate the presence of significant local grain misorientations (typical of high local densities of geometrically necessary dislocations) near HCP precipitates and BCC_1/BCC_2 interfaces. This may be because the dislocation microstructures, accommodating the misfit between these phases, may be relaxed at 900 °C into low energy configurations with no net shear strain, which are not visible in the KAM maps.

These points deserve further investigations with a more sophisticated approach, for example phase field. However, the latter is out of the scope of the present study.

4. Conclusions

Initially homogeneous and single-phase BCC HfNbTaTiZr samples with similar grain sizes (50 - 70 μm) were aged at 900 °C for 10 or 1000 h to investigate their phase stability. The three considered states included (1) an HfNbTaTiZr alloy that was either annealed under a controlled Ar atmosphere or (2) contaminated by O during aging, and (3) a HEA doped with 3 at.% O heat treated in Ar. The key results of this work are summarized below:

(1) The HfNbTaTiZr alloy forms a stable BCC solid solution at 900 °C. It remains in this state even after a heat treatment of 1000 h at this temperature. However, if the alloy is contaminated by O from the atmosphere during the heat treatment, a monotectoid reaction is promoted with the formation of two phases into a Zr-Hf-rich HCP phase and a Nb-Ta-rich BCC phase.

(2) In most of the cases, the OR between the HCP phase and the BCC phases is in line with that of Burgers (110)BCC || (0001)HCP and $[1\bar{1}1]$BCC || $[11\bar{2}0]$HCP. In a few cases, we also identified the following ORs at moving grain boundaries and near triple junctions: $(\bar{1}10)$BCC || $(\bar{1}011)$HCP and [113]BCC || $[11\bar{2}3]$HCP as well as (021)BCC || (0001)HCP and [100]BCC || $[2\bar{1}\bar{1}0]$HCP.

(3) Two precipitate morphologies were identified in the O-contaminated alloy. The first one resembles that forming because of discontinuous precipitation, i.e., the growth of precipitates seems to be related to grain boundary migration. The second morphology consists of colonies of elongated and nearly parallel precipitates. Depending on the angle with which these rod-like precipitates intersect the sample surface, they either appear as needles or dots.

(4) While some grain boundaries were found to be fully covered by precipitates, some others were completely devoid of precipitates. In the latter case, a detailed analysis revealed that these boundaries are special CSL boundaries with potential low interfacial energies. Due to their typically higher packing factor compared to other arbitrary high-angle grain boundaries, transport along CSL boundaries is slower and CSL boundaries are less potent for the nucleation of secondary phases.

(5) Within colonies, the elongated and approximately parallel HCP rods (deviations of up to 20°) grow along directions comprised between ⟨311⟩BCC and ⟨100⟩BCC. Our calculations suggest that

the precipitates should grow preferentially along ⟨100⟩BCC, for which the density of elastic strain energy is minimum. One possibility to rationalize the observed deviation is as follows. The precipitates initially grow along ⟨100⟩BCC but the large misfit between the BCC and HCP phases may be accommodated by bulk plasticity and/or interfacial dislocations, thus inducing the deviation from this direction towards ⟨311⟩BCC.

Research data for this article

The research data of the present article can be found on the following Mendeley data repository: https://data.mendeley.com/preview/tng4s6n4v3?a=3a7d65ee-54d8–4b84–81d2–4d77f0b9db09

CRediT authorship contribution statement

Régis Poulain: Data curation, Formal analysis, Investigation, Visualization, Writing – original draft, Writing – review & editing, Software. **Maik Rajkowski:** Data curation, Formal analysis, Investigation, Writing – review & editing, Validation. **Yujun Zhao:** Data curation, Formal analysis, Investigation, Writing – review & editing, Validation. **Parham Gemagami:** Data curation, Formal analysis, Investigation, Validation. **Benoît Appolaire:** Data curation, Formal analysis, Investigation, Software, Visualization, Writing – original draft, Writing – review & editing. **Stephan Laube:** Investigation, Writing – review & editing, Resources. **Alexander Kauffmann:** Investigation, Writing – review & editing, Resources. **Loïc Perrière:** Investigation, Writing – review & editing, Resources. **Jean-Philippe Couzinié:** Funding acquisition, Investigation, Software, Writing – review & editing, Resources. **Tong Li:** Conceptualization, Funding acquisition, Project administration, Supervision, Writing – review & editing. **Guillaume Laplanche:** Conceptualization, Funding acquisition, Methodology, Project administration, Supervision, Writing – original draft, Writing – review & editing.

Declaration of competing interest

The authors declare that they have no known competing financial interests or personal relationships that could have appeared to influence the work reported in this paper.

Acknowledgments

GL and TL acknowledge funding from the German Research Foundation (Deutsche Forschungsgemeinschaft DFG) through projects LA 3607/3–2 and TL 3272/6–2 (common project number 388735491) in the framework of the Priority Program SPP 2006 “Compositionally Complex Alloys – High Entropy Alloys”. RP, LP and JPC would like to acknowledge funding from INC—CNRS through the International Emerging Action (IEA) n°487. The Center for interface-dominated high-performance materials (Zentrum für Grenzflachendominierte Höchstleistungswerkstoffe, ZGH) is acknowledged for the use of the Buehler Vibromet 2 and the JEOL JSM-7200F SEM. Hans Chen is acknowledge for his experimental support in the early stages of this research and Jens Freudenberger is acknowledged for his attempt to cold work the O-doped alloy by rotary swaging. After a diameter reduction of ~40 %, cracks were found to form in the material and therefore, this material state was not further considered in the present work.

Supplementary materials

Supplementary material associated with this article can be found, in the online version, at doi:10.1016/j.actamat.2024.120295.

References

[1] O.N. Senkov, J.M. Scott, S.V. Senkova, D.B. Miracle, C.F. Woodward, Microstructure and room temperature properties of a high-entropy TaNbHfZrTi alloy, J. Alloys Compd. 509 (2011) 6043–6048, https://doi.org/10.1016/j.jallcom.2011.02.171.

[2] O.N. Senkov, J.M. Scott, S.V. Senkova, F. Meisenkothen, D.B. Miracle, C. F. Woodward, Microstructure and elevated temperature properties of a refractory TaNbHfZrTi alloy, J. Mater. Sci. 47 (2012) 4062–4074, https://doi.org/10.1007/s10853-012-6260-2.

[3] O.N. Senkov, S.L. Semiatin, Microstructure and properties of a refractory high-entropy alloy after cold working, J. Alloys Compd. 649 (2015) 1110–1123, https://doi.org/10.1016/j.jallcom.2015.07.209.

[4] B. Schuh, B. Völker, J. Todt, N. Schell, L. Perrière, J. Li, J. Couzinié, A. Hohenwarter, Thermodynamic instability of a nanocrystalline, single-phase TiZrNbHfTa alloy and its impact on the mechanical properties, Acta Mater. 142 (2018) 201–212, https://doi.org/10.1016/j.actamat.2017.09.035.

[5] J. Čížek, P. Haušild, M. Cieslar, O. Melikhova, T. Vlasák, M. Janeček, R. Král, P. Harcuba, F. Lukáč, J. Zýka, J. Málek, J. Moon, H.S. Kim, Strength enhancement of high entropy alloy HfNbTaTiZr by severe plastic deformation, J. Alloys Compd. 768 (2018) 924–937, https://doi.org/10.1016/j.jallcom.2018.07.319.

[6] F. Lukac, M. Dudr, R. Musalek, J. Klecka, J. Cinert, J. Cizek, T. Chraska, J. Cizek, O. Melikhova, J. Kuriplach, Spark plasma sintering of gas atomized high-entropy alloy HfNbTaTiZr, J. Mater. Res. 33 (2018) 3247–3257, https://doi.org/10.1557/jmr.2018.320.

[7] H. Dobbelstein, E.L. Gurevich, E.P. George, A. Ostendorf, G. Laplanche, Laser metal deposition of a refractory TiZrNbHfTa high-entropy alloy, Addit. Manuf. 24 (2018) 386–390, https://doi.org/10.1016/j.addma.2018.10.008.

[8] H. Dobbelstein, E.P. George, E.L. Gurevich, A. Kostka, A. Ostendorf, G. Laplanche, Laser metal deposition of refractory high-entropy alloys for high-throughput synthesis and structure-property characterization, Int. J. Extreme Manuf. 3 (2021) 015201, https://doi.org/10.1088/2631-7990/abcca8.

[9] X. Yuan, Y. Wu, M. Zhou, X. Liu, H. Wang, S. Jiang, X. Zhang, H. Wu, X. Liu, Z. Chen, X. Xu, Z. Lu, Effects of trace elements on mechanical properties of the TiZrHfNb high-entropy alloy, J. Mater. Sci. Technol. 152 (2023) 135–147, https://doi.org/10.1016/j.jmst.2022.12.025.

[10] É. Fazakas, V. Zadorozhnyy, L.K. Varga, A. Inoue, D.V. Louzguine-Luzgin, F. Tian, L. Vitos, Experimental and theoretical study of $Ti_{20}Zr_{20}Hf_{20}Nb_{20}X_{20}$ (X = V or Cr) refractory high-entropy alloys, Int. J. Refractory Metals Hard Mater. 47 (2014) 131–138, https://doi.org/10.1016/j.ijrmhm.2014.07.009.

[11] G. Dirras, L. Lilensten, P. Djemia, M. Laurent-Brocq, D. Tingaud, J.P. Couzinié, L. Perrière, T. Chauveau, I. Guillot, Elastic and plastic properties of as-cast equimolar TiHfZrTaNb high-entropy alloy, Mater. Sci. Eng. A 654 (2016) 30–38, https://doi.org/10.1016/j.msea.2015.12.017.

[12] H. Song, F. Tian, D. Wang, Thermodynamic properties of refractory high entropy alloys, J. Alloys Compd. 682 (2016) 773–777, https://doi.org/10.1016/j.jallcom.2016.04.320.

[13] G. Laplanche, P. Gadaud, L. Perrière, I. Guillot, J.P. Couzinié, Temperature dependence of elastic moduli in a refractory HfNbTaTiZr high-entropy alloy, J. Alloys Compd. 799 (2019) 538–545, https://doi.org/10.1016/j.jallcom.2019.05.322.

[14] J.P. Couzinié, L. Lilensten, Y. Champion, G. Dirras, L. Perrière, I. Guillot, On the room temperature deformation mechanisms of a TiZrHfNbTa refractory high-entropy alloy, Mater. Sci. Eng. A 645 (2015) 255–263, https://doi.org/10.1016/j.msea.2015.08.024.

[15] G. Dirras, H. Couque, L. Lilensten, A. Heczel, D. Tingaud, J.P. Couzinié, L. Perrière, J. Gubicza, I. Guillot, Mechanical behavior and microstructure of $Ti_{20}Hf_{20}Zr_{20}Ta_{20}Nb_{20}$ high-entropy alloy loaded under quasi-static and dynamic compression conditions, Mater. Charact. 111 (2016) 106–113, https://doi.org/10.1016/j.matchar.2015.11.018.

[16] L. Lilensten, J.-P. Couzinié, L. Perrière, A. Hocini, C. Keller, G. Dirras, I. Guillot, Study of a bcc multi-principal element alloy: tensile and simple shear properties and underlying deformation mechanisms, Acta Mater. 142 (2018) 131–141, https://doi.org/10.1016/j.actamat.2017.09.062.

[17] M.A. Charpagne, J.C. Stinville, F. Wang, N. Philips, T.M. Pollock, Orientation dependent plastic localization in the refractory high entropy alloy HfNbTaTiZr at room temperature, Mater. Sci. Eng. 848 (2022) 143291, https://doi.org/10.1016/j.msea.2022.143291.

[18] C.-C. Juan, M.-H. Tsai, C.-W. Tsai, W.-L. Hsu, C.-M. Lin, S.-K. Chen, S.-J. Lin, J.-W. Yeh, Simultaneously increasing the strength and ductility of a refractory high-entropy alloy via grain refining, Mater. Lett. 184 (2016) 200–203, https://doi.org/10.1016/j.matlet.2016.08.060.

[19] R.R. Eleti, T. Bhattacharjee, A. Shibata, N. Tsuji, Unique deformation behavior and microstructure evolution in high temperature processing of HfNbTaTiZr refractory high entropy alloy, Acta Mater. 171 (2019) 132–145, https://doi.org/10.1016/j.actamat.2019.04.018.

[20] R.R. Eleti, A.H. Chokshi, A. Shibata, N. Tsuji, Unique high-temperature deformation dominated by grain boundary sliding in heterogeneous necklace structure formed by dynamic recrystallization in HfNbTaTiZr BCC refractory high entropy alloy, Acta Mater. 183 (2020) 64–77, https://doi.org/10.1016/j.actamat.2019.11.001.

[21] C.-J. Liu, C. Gadelmeier, S.-L. Lu, J.-W. Yeh, H.-W. Yen, S. Gorsse, U. Glatzel, A.-C. Yeh, Tensile creep behavior of HfNbTaTiZr refractory high entropy alloy at elevated temperatures, Acta Mater. 237 (2022) 118188, https://doi.org/10.1016/j.actamat.2022.118188.

[22] L.H. Mills, M.G. Emigh, C.H. Frey, N.R. Philips, S.P. Murray, J. Shin, D.S. Gianola, T.M. Pollock, Temperature-dependent tensile behavior of the HfNbTaTiZr multi-principal element alloy, Acta Mater. 245 (2023) 118618, https://doi.org/10.1016/j.actamat.2022.118618.
[23] H. Chen, T. Hanemann, S. Seils, D. Schliephake, A.S. Tirunilai, M. Heilmaier, K.-P. Weiss, A. Kauffmann, Influence of temperature and plastic strain on deformation mechanisms and kink band formation in homogenized HfNbTaTiZr, Crystals 11 (2021) 81, https://doi.org/10.3390/cryst11020081.
[24] J. Zhang, C. Gadelmeier, S. Sen, R. Wang, X. Zhang, Y. Zhong, U. Glatzel, B. Grabowski, G. Wilde, S.V. Divinski, Zr diffusion in BCC refractory high entropy alloys: a case of 'non-sluggish' diffusion behavior, Acta Mater. 233 (2022) 117970, https://doi.org/10.1016/j.actamat.2022.117970.
[25] P. Hruška, F. Lukáč, S. Cichoň, M. Vondráček, J. Čížek, L. Fekete, J. Lančok, J. Veselý, P. Minárik, M. Cieslar, O. Melikhova, T. Kmječ, M.O. Liedke, M. Butterling, A. Wagner, Oxidation of amorphous HfNbTaTiZr high entropy alloy thin films prepared by DC magnetron sputtering, J. Alloys Compd. 869 (2021) 157978, https://doi.org/10.1016/j.jallcom.2020.157978.
[26] D. Dickes, B. Öztürk, F. Baier, P. Berger, E.P. George, R. Völkl, M.C. Galetz, U. Glatzel, Surface hardening of TiZrNbHfTa high entropy alloy via oxidation, Corros. Sci. 217 (2023) 111159, https://doi.org/10.1016/j.corsci.2023.111159.
[27] S.Y. Chen, Y. Tong, K.K. Tseng, J.W. Yeh, J.D. Poplawsky, J.G. Wen, M.C. Gao, G. Kim, W. Chen, Y. Ren, R. Feng, W.D. Li, P.K. Liaw, Phase transformations of HfNbTaTiZr high-entropy alloy at intermediate temperatures, Scr. Mater. 158 (2019) 50–56, https://doi.org/10.1016/j.scriptamat.2018.08.032.
[28] N.D. Stepanov, N.Y. Yurchenko, S.V. Zherebtsov, M.A. Tikhonovsky, G. A. Salishchev, Aging behavior of the HfNbTaTiZr high entropy alloy, Mater. Lett. 211 (2018) 87–90, https://doi.org/10.1016/j.matlet.2017.09.094.
[29] C. Yang, K. Aoyagi, H. Bian, A. Chiba, Microstructure evolution and mechanical property of a precipitation-strengthened refractory high-entropy alloy HfNbTaTiZr, Mater. Lett. 254 (2019) 46–49, https://doi.org/10.1016/j.matlet.2019.07.027.
[30] S. Maiti, W. Steurer, Structural-disorder and its effect on mechanical properties in single-phase TaNbHfZr high-entropy alloy, Acta Mater. 106 (2016) 87–97, https://doi.org/10.1016/j.actamat.2016.01.018.
[31] W.G. Burgers, On the process of transition of the cubic-body-centered modification into the hexagonal-close-packed modification of zirconium, Physica 1 (1934) 561–586, https://doi.org/10.1016/S0031-8914(34)80244-3.
[32] J.P. Couzinié, G. Dirras, L. Perrière, T. Chauveau, E. Leroy, Y. Champion, I. Guillot, Microstructure of a near-equimolar refractory high-entropy alloy, Mater. Lett. 126 (2014) 285–287, https://doi.org/10.1016/j.matlet.2014.04.062.
[33] F. Bachmann, R. Hielscher, H. Schaeben, Texture analysis with MTEX – free and open source software toolbox, Solid State Phenomena 160 (2010) 63–68, https://doi.org/10.4028/www.scientific.net/SSP.160.63.
[34] A.G. Khachaturyan, Theory of Structural Transformation in Solids, John Wiley & Sons1983.
[35] M. Cottura, B. Appolaire, A. Finel, Y.L. Bouar, Phase field study of acicular growth: role of elasticity in Widmanstätten structure, Acta Mater. 72 (2014) 200–210, https://doi.org/10.1016/j.actamat.2014.03.045.
[36] H. Lebbad, B. Appolaire, Y.L. Bouar, A. Finel, Insights into the selection mechanism of Widmanstätten growth by phase-field calculations, Acta Mater. 217 (2021) 117148, https://doi.org/10.1016/j.actamat.2021.117148.
[37] E.S. Fisher, C.J. Renken, Single-crystal elastic moduli and the hcp → bcc transformation in Ti, Zr, and Hf, Phys. Rev. 135 (1964) A482–A494, https://doi.org/10.1103/PhysRev.135.A482.
[38] E. Walker, P. Bujard, Anomalous temperature behaviour of the shear elastic constant C44 in tantalum, Solid State Commun. 34 (1980) 691–693, https://doi.org/10.1016/0038-1098(80)90957-6.
[39] D.A. Porter, K.E. Easterling, M. Sherif, Phase Transformations in Metals and Alloys, Third Edition (Revised Reprint), 3rd ed., CRC Press, Hoboken, 2009.
[40] H. Mehrer, Diffusion in Solids: Fundamentals, Methods, Materials, Diffusion-Controlled Processes, Springer Science & Business Media, 2007.
[41] D. Dickes, Y. Zhao, F. Baier, B. Öztürk, R. Völkl, T. Li, M.C. Galetz, U. Glatzel, Influence of oxygen ingress on microstructure and phase formation during two-step oxidation surface hardening of TiZrNbHfTa high entropy alloy, Appl. Phys. Lett. 124 (2024), https://doi.org/10.1063/5.0190771.
[42] C.H. Belcher, B.E. MacDonald, D. Apelian, E.J. Lavernia, The role of interstitial constituents in refractory complex concentrated alloys, Prog. Mater. Sci. 137 (2023) 101140, https://doi.org/10.1016/j.pmatsci.2023.101140.
[43] G.F. Vander Voort, S.R. Lampman, B.R. Sanders, G.J. Anton, C. Polakowski, J. Kinson, K. Muldoon, S.D. Henry, W.W. Scott Jr, ASM Handbook, 2004.
[44] I. Manna, S.K. Pabi, W. Gust, Discontinuous reactions in solids, Int. Mater. Rev. 46 (2001) 53–91, https://doi.org/10.1179/095066001101528402.
[45] P. Zięba, Recent developments on discontinuous precipitation, Arch. Metal. Mater. 62 (2017), https://doi.org/10.1515/amm-2017-0138.
[46] H. Okamoto, Hf-Ta (hafnium-tantalum), J. Phase Equilibria 17 (1996), https://doi.org/10.1007/BF02648500, 270-270.
[47] H. Okamoto, Nb-Zr (niobium-zirconium), J. Phase Equilibria 13 (1992), https://doi.org/10.1007/BF02665776, 577-577.
[48] H. Okamoto, Ta-Zr (tantalum-zirconium), J. Phase Equilibria 17 (1996), https://doi.org/10.1007/BF02666009, 555-555.
[49] T.B. Massalski, J.L. Murray, L.H. Bennett, H. Baker, Binary Alloy Phase Diagrams, American Society for Metals (ASM), 1986.
[50] S. Barzilai, C. Toher, S. Curtarolo, O. Levy, Evaluation of the tantalum-titanium phase diagram from ab-initio calculations, Acta Mater. 120 (2016) 255–263, https://doi.org/10.1016/j.actamat.2016.08.053.
[51] M. Bönisch, M. Stoica, M. Calin, Routes to control diffusive pathways and thermal expansion in Ti-alloys, Sci. Rep. 10 (2020) 3045, https://doi.org/10.1038/s41598-020-60038-x.
[52] R.J. Pérez, A.R. Massih, Thermodynamic evaluation of the Nb–O–Zr system, J. Nucl. Mater. 360 (2007) 242–254, https://doi.org/10.1016/j.jnucmat.2006.10.008.
[53] Y. Ishiguro, Y. Tsukada, T. Koyama, Phase-field study of the spinodal decomposition rate of β phase in oxygen-added Ti–Nb alloys, Comput. Mater. Sci. 174 (2020) 109471, https://doi.org/10.1016/j.commatsci.2019.109471.
[54] D.E. Coates, Diffusion-controlled precipitate growth in ternary systems I, Metal. Trans. 3 (1972) 1203–1212, https://doi.org/10.1007/BF02642453.
[55] D.H. Warrington, P. Bufalini, The coincidence site lattice and grain boundaries, Scripta Metallurgica 5 (1971) 771–776, https://doi.org/10.1016/0036-9748(71)90161-X.
[56] V. Randle, The coincidence site lattice and the 'sigma enigma, Mater. Charact. 47 (2001) 411–416, https://doi.org/10.1016/S1044-5803(02)00193-6.
[57] D. Bhattacharyya, G.B. Viswanathan, R. Denkenberger, D. Furrer, H.L. Fraser, The role of crystallographic and geometrical relationships between α and β phases in an α/β titanium alloy, Acta Mater. 51 (2003) 4679–4691, https://doi.org/10.1016/S1359-6454(03)00179-4.
[58] J. Dai, H. Guan, L. Chai, K. Xiang, Y. Zhu, R. Qiu, N. Guo, Y. Liu, Comparative Study of Microstructural Characteristics and Hardness of β-Quenched Zr702 and Zr–2.5Nb Alloys, Materials. (Basel) 12 (2019) 3752, https://doi.org/10.3390/ma12223752.
[59] M.X. Zhang, P.M. Kelly, Edge-to-edge matching and its applications: part I. Application to the simple HCP/BCC system, Acta Mater. 53 (2005) 1073–1084, https://doi.org/10.1016/j.actamat.2004.11.007.
[60] W. Rong, G.L. Dunlop, The crystallography of secondary carbide precipitation in high speed steel, Acta Metal. 32 (1984) 1591–1599, https://doi.org/10.1016/0001-6160(84)90218-9.
[61] A. Settefrati, E. Aeby-Gautier, M. Dehmas, G. Geandier, B. Appolaire, S. Audion, J. Delfosse, Precipitation in a near beta titanium alloy on ageing: influence of heating rate and chemical composition of the beta-metastable phase, Solid State Phenomena 172 (2011) 760–765, https://doi.org/10.4028/www.scientific.net/SSP.172-174.760.
[62] B. Appolaire, A. Settefrati, E. Aeby-Gautier, Stress and strain fields associated with the formation of α" in near-β titanium alloys, Mater. Today 2 (2015) S589–S592, https://doi.org/10.1016/j.matpr.2015.07.353.